hep-ex/9504004
DESY 95-062
April 1995

ISSN 0418-9833

hep-ex/9504004 v2 12 Apr 1995

# Inclusive Parton Cross Sections in Photoproduction and Photon Structure

H1 Collaboration

**Abstract:**

Photoproduction of 2-jet events is studied with the H1 detector at HERA. Parton cross sections are extracted from the data by an unfolding method using leading order parton-jet correlations of a QCD generator. The gluon distribution in the photon is derived in the fractional momentum range $0.04 \leq x_\gamma \leq 1$ at the average factorization scale 75 GeV$^2$.

# H1 Collaboration

T. Ahmed[3], S. Aid[13], V. Andreev[24], B. Andrieu[28], R.-D. Appuhn[11], M. Arpagaus[36],
A. Babaev[26], J. Baehr[35], J. Bán[17], Y. Ban[27], P. Baranov[24], E. Barrelet[29], W. Bartel[11],
M. Barth[4], U. Bassler[29], H.P. Beck[37], H.-J. Behrend[11], A. Belousov[24], Ch. Berger[1],
G. Bernardi[29], R. Bernet[36], G. Bertrand-Coremans[4], M. Besançon[9], R. Beyer[11], P. Biddulph[22],
P. Bispham[22], J.C. Bizot[27], V. Blobel[13], K. Borras[8], F. Botterweck[4], V. Boudry[7],
A. Braemer[14], F. Brasse[11], W. Braunschweig[1], V. Brisson[27], D. Bruncko[17], C. Brune[15],
R.Buchholz[11], L. Büngener[13], J. Bürger[11], F.W. Büsser[13], A. Buniatian[11,38], S. Burke[18],
M. Burton[22], G. Buschhorn[26], A.J. Campbell[11], T. Carli[26], F. Charles[11], M. Charlet[11],
D. Clarke[5], A.B. Clegg[18], B. Clerbaux[4], M. Colombo[8], J.G. Contreras[8], C. Cormack[19],
J.A. Coughlan[5], A. Courau[27], Ch. Coutures[9], G. Cozzika[9], L. Criegee[11], D.G. Cussans[5],
J. Cvach[30], S. Dagoret[29], J.B. Dainton[19], W.D. Dau[16], K. Daum[34], M. David[9], B. Delcourt[27],
L. Del Buono[29], A. De Roeck[11], E.A. De Wolf[4], P. Di Nezza[32], C. Dollfus[37], J.D. Dowell[3],
H.B. Dreis[2], A. Droutskoi[23], J. Duboc[29], D. Düllmann[13], O. Dünger[13], H. Duhm[12], J. Ebert[34],
T.R. Ebert[19], G. Eckerlin[11], V. Efremenko[23], S. Egli[37], H. Ehrlichmann[35], S. Eichenberger[37],
R. Eichler[36], F. Eisele[14], E. Eisenhandler[20], R.J. Ellison[22], E. Elsen[11], M. Erdmann[14],
W. Erdmann[36], E. Evrard[4], L. Favart[4], A. Fedotov[23], D. Feeken[13], R. Felst[11], J. Feltesse[9],
J. Ferencei[15], F. Ferrarotto[32], K. Flamm[11], M. Fleischer[11], M. Flieser[26], G. Flügge[2],
A. Fomenko[24], B. Fominykh[23], M. Forbush[7], J. Formánek[31], J.M. Foster[22], G. Franke[11],
E. Fretwurst[12], E. Gabathuler[19], K. Gabathuler[33], K. Gamerdinger[26], J. Garvey[3], J. Gayler[11],
M. Gebauer[8], A. Gellrich[11], H. Genzel[1], R. Gerhards[11], U. Goerlach[11], L. Goerlich[6],
N. Gogitidze[24], M. Goldberg[29], D. Goldner[8], B. Gonzalez-Pineiro[29], I. Gorelov[23],
P. Goritchev[23], C. Grab[36], H. Grässler[2], R. Grässler[2], T. Greenshaw[19], G. Grindhammer[26],
A. Gruber[26], C. Gruber[16], J. Haack[35], D. Haidt[11], L. Hajduk[6], O. Hamon[29], M. Hampel[1],
E.M. Hanlon[18], M. Hapke[11], W.J. Haynes[5], J. Heatherington[20], G. Heinzelmann[13],
R.C.W. Henderson[18], H. Henschel[35], I. Herynek[30], M.F. Hess[26], W. Hildesheim[11], P. Hill[5],
K.H. Hiller[35], C.D. Hilton[22], J. Hladký[30], K.C. Hoeger[22], M. Höppner[8], R. Horisberger[33],
V.L. Hudgson[3], Ph. Huet[4], M. Hütte[8], H. Hufnagel[14], M. Ibbotson[22], H. Itterbeck[1],
M.-A. Jabiol[9], A. Jacholkowska[27], C. Jacobsson[21], M. Jaffre[27], J. Janoth[15], T. Jansen[11],
L. Jönsson[21], D.P. Johnson[4], L. Johnson[18], H. Jung[29], P.I.P. Kalmus[20], D. Kant[20],
R. Kaschowitz[2], P. Kasselmann[12], U. Kathage[16], J. Katzy[14], H.H. Kaufmann[35], S. Kazarian[11],
I.R. Kenyon[3], S. Kermiche[25], C. Keuker[1], C. Kiesling[26], M. Klein[35], C. Kleinwort[13],
G. Knies[11], W. Ko[7], T. Köhler[1], J.H. Köhne[26], H. Kolanoski[8], F. Kole[7], S.D. Kolya[22],
V. Korbel[11], M. Korn[8], P. Kostka[35], S.K. Kotelnikov[24], T. Krämerkämper[8], M.W. Krasny[6,29],
H. Krehbiel[11], D. Krücker[2], U. Krüger[11], U. Krüner-Marquis[11], J.P. Kubenka[26], H. Küster[2],
M. Kuhlen[26], T. Kurča[17], J. Kurzhöfer[8], B. Kuznik[34], D. Lacour[29], F. Lamarche[28],
R. Lander[7], M.P.J. Landon[20], W. Lange[35], P. Lanius[26], J.-F. Laporte[9], A. Lebedev[24],
C. Leverenz[11], S. Levonian[24], Ch. Ley[2], A. Lindner[8], G. Lindström[12], J. Link[7], F. Linsel[11],
J. Lipinski[13], B. List[11], G. Lobo[27], P. Loch[27], H. Lohmander[21], J. Lomas[22], G.C. Lopez[20],
V. Lubimov[23], D. Lüke[8,11], N. Magnussen[34], E. Malinovski[24], S. Mani[7], R. Maraček[17],
P. Marage[4], J. Marks[25], R. Marshall[22], J. Martens[34], R. Martin[11], H.-U. Martyn[1],
J. Martyniak[6], S. Masson[2], T. Mavroidis[20], S.J. Maxfield[19], S.J. McMahon[19], A. Mehta[22],
K. Meier[15], D. Mercer[22], T. Merz[11], C.A. Meyer[37], H. Meyer[34], J. Meyer[11], A. Migliori[28],
S. Mikocki[6], D. Milstead[19], F. Moreau[28], J.V. Morris[5], E. Mroczko[6], G. Müller[11], K. Müller[11],
P. Murín[17], V. Nagovizin[23], R. Nahnhauer[35], B. Naroska[13], Th. Naumann[35], P.R. Newman[3],
D. Newton[18], D. Neyret[29], H.K. Nguyen[29], T.C. Nicholls[3], F. Niebergall[13], C. Niebuhr[11],
Ch. Niedzballa[1], R. Nisius[1], G. Nowak[6], G.W. Noyes[5], M. Nyberg-Werther[21], M. Oakden[19],
H. Oberlack[26], U. Obrock[8], J.E. Olsson[11], D. Ozerov[23], E. Panaro[11], A. Panitch[4],
C. Pascaud[27], G.D. Patel[19], E. Peppel[35], E. Perez[9], J.P. Phillips[22], Ch. Pichler[12],
A. Pieuchot[25], D. Pitzl[36], G. Pope[7], S. Prell[11], R. Prosi[11], K. Rabbertz[1], G. Rädel[11],
F. Raupach[1], P. Reimer[30], S. Reinshagen[11], P. Ribarics[26], H.Rick[8], V. Riech[12],

J. Riedlberger[36], S. Riess[13], M. Rietz[2], E. Rizvi[20], S.M. Robertson[3], P. Robmann[37], H.E. Roloff[35], R. Roosen[4], K. Rosenbauer[1] A. Rostovtsev[23], F. Rouse[7], C. Royon[9], K. Rüter[26], S. Rusakov[24], K. Rybicki[6], R. Rylko[20], N. Sahlmann[2], S.G. Salesch[11], E. Sanchez[26], D.P.C. Sankey[5], P. Schacht[26], S. Schiek[11], P. Schleper[14], W. von Schlippe[20], C. Schmidt[11], D. Schmidt[34], G. Schmidt[13], A. Schöning[11], V. Schröder[11], E. Schuhmann[26], B. Schwab[14], A. Schwind[35], F. Sefkow[11], M. Seidel[12], R. Sell[11], A. Semenov[23], V. Shekelyan[11], I. Sheviakov[24], H. Shooshtari[26], L.N. Shtarkov[24], G. Siegmon[16], U. Siewert[16], Y. Sirois[28], I.O. Skillicorn[10], P. Smirnov[24], J.R. Smith[7], V. Solochenko[23], Y. Soloviev[24], J. Spiekermann[8], S. Spielman[28], H. Spitzer[13], R. Starosta[1], M. Steenbock[13], P. Steffen[11], R. Steinberg[2], B. Stella[32], K. Stephens[22], J. Stier[11], J. Stiewe[15], U. Stösslein[35], K. Stolze[35], J. Strachota[30], U. Straumann[37], W. Struczinski[2], J.P. Sutton[3], S. Tapprogge[15], V. Tchernyshov[23], C. Thiebaux[28], G. Thompson[20], P. Truöl[37], J. Turnau[6], J. Tutas[14], P. Uelkes[2], A. Usik[24], S. Valkár[31], A. Valkárová[31], C. Vallée[25], P. Van Esch[4], P. Van Mechelen[4], A. Vartapetian[11,38], Y. Vazdik[24], P. Verrecchia[9], G. Villet[9], K. Wacker[8], A. Wagener[2], M. Wagener[33], I.W. Walker[18], A. Walther[8], G. Weber[13], M. Weber[11], D. Wegener[8], A. Wegner[11], H.P. Wellisch[26], L.R. West[3], S. Willard[7], M. Winde[35], G.-G. Winter[11], C. Wittek[13], A.E. Wright[22], E. Wünsch[11], N. Wulff[11], T.P. Yiou[29], J. Žáček[31], D. Zarbock[12], Z. Zhang[27], A. Zhokin[23], M. Zimmer[11], W. Zimmermann[11], F. Zomer[27], and K. Zuber[15]

[1] *I. Physikalisches Institut der RWTH, Aachen, Germany*[a]
[2] *III. Physikalisches Institut der RWTH, Aachen, Germany*[a]
[3] *School of Physics and Space Research, University of Birmingham, Birmingham, UK*[b]
[4] *Inter-University Institute for High Energies ULB-VUB, Brussels; Universitaire Instelling Antwerpen, Wilrijk, Belgium*[c]
[5] *Rutherford Appleton Laboratory, Chilton, Didcot, UK*[b]
[6] *Institute for Nuclear Physics, Cracow, Poland*[d]
[7] *Physics Department and IIRPA, University of California, Davis, California, USA*[e]
[8] *Institut für Physik, Universität Dortmund, Dortmund, Germany*[a]
[9] *CEA, DSM/DAPNIA, CE-Saclay, Gif-sur-Yvette, France*
[10] *Department of Physics and Astronomy, University of Glasgow, Glasgow, UK*[b]
[11] *DESY, Hamburg, Germany*[a]
[12] *I. Institut für Experimentalphysik, Universität Hamburg, Hamburg, Germany*[a]
[13] *II. Institut für Experimentalphysik, Universität Hamburg, Hamburg, Germany*[a]
[14] *Physikalisches Institut, Universität Heidelberg, Heidelberg, Germany*[a]
[15] *Institut für Hochenergiephysik, Universität Heidelberg, Heidelberg, Germany*[a]
[16] *Institut für Reine und Angewandte Kernphysik, Universität Kiel, Kiel, Germany*[a]
[17] *Institute of Experimental Physics, Slovak Academy of Sciences, Košice, Slovak Republic*[f]
[18] *School of Physics and Materials, University of Lancaster, Lancaster, UK*[b]
[19] *Department of Physics, University of Liverpool, Liverpool, UK*[b]
[20] *Queen Mary and Westfield College, London, UK*[b]
[21] *Physics Department, University of Lund, Lund, Sweden*[g]
[22] *Physics Department, University of Manchester, Manchester, UK*[b]
[23] *Institute for Theoretical and Experimental Physics, Moscow, Russia*
[24] *Lebedev Physical Institute, Moscow, Russia*[f]
[25] *CPPM, Université d'Aix-Marseille II, IN2P3-CNRS, Marseille, France*
[26] *Max-Planck-Institut für Physik, München, Germany*[a]
[27] *LAL, Université de Paris-Sud, IN2P3-CNRS, Orsay, France*
[28] *LPNHE, Ecole Polytechnique, IN2P3-CNRS, Palaiseau, France*
[29] *LPNHE, Universités Paris VI and VII, IN2P3-CNRS, Paris, France*
[30] *Institute of Physics, Czech Academy of Sciences, Praha, Czech Republic*[f,h]
[31] *Nuclear Center, Charles University, Praha, Czech Republic*[f,h]
[32] *INFN Roma and Dipartimento di Fisica, Universita "La Sapienza", Roma, Italy*

[33] *Paul Scherrer Institut, Villigen, Switzerland*
[34] *Fachbereich Physik, Bergische Universität Gesamthochschule Wuppertal, Wuppertal, Germany*[a]
[35] *DESY, Institut für Hochenergiephysik, Zeuthen, Germany*[a]
[36] *Institut für Teilchenphysik, ETH, Zürich, Switzerland*[i]
[37] *Physik-Institut der Universität Zürich, Zürich, Switzerland*[i]
[38] *Visitor from Yerevan Phys.Inst., Armenia*

[a] *Supported by the Bundesministerium für Forschung und Technologie, FRG under contract numbers 6AC17P, 6AC47P, 6DO57I, 6HH17P, 6HH27I, 6HD17I, 6HD27I, 6KI17P, 6MP17I, and 6WT87P*
[b] *Supported by the UK Particle Physics and Astronomy Research Council, and formerly by the UK Science and Engineering Research Council*
[c] *Supported by FNRS-NFWO, IISN-IIKW*
[d] *Supported by the Polish State Committee for Scientific Research, grant No. 204209101*
[e] *Supported in part by USDOE grant DE F603 91ER40674*
[f] *Supported by the Deutsche Forschungsgemeinschaft*
[g] *Supported by the Swedish Natural Science Research Council*
[h] *Supported by GA ČR, grant no. 202/93/2423 and by GA AV ČR, grant no. 19095*
[i] *Supported by the Swiss National Science Foundation*

# 1 Introduction

The interaction of electrons and protons at the HERA collider is dominated by photoproduction processes: electrons scatter through small angles and emit quasi-real photons, which then interact with the protons. The center of mass (CMS) energies in the $\gamma p$ system reach up to 300 GeV. A fraction of these events has large transverse energy in the final state including the formation of jets, as has been reported in several recent publications [1, 2, 3].

The jet production can be well described in the framework of QCD. In this picture the photon couples either directly to a parton of the proton, or indirectly via the photon's own parton content. The first are called *direct* processes, which include the QCD-Compton (Fig.1a) and photon-gluon fusion diagrams, while the latter are usually refered to as *resolved* processes. An example is shown in Fig. 1b.

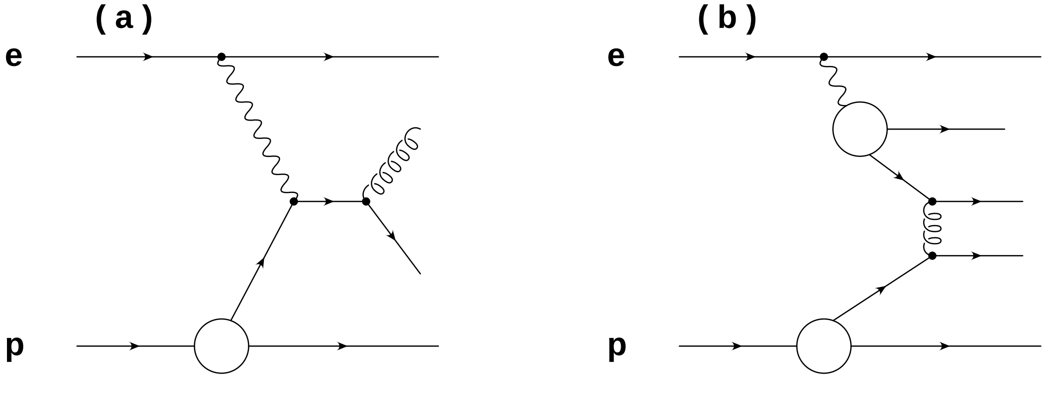

**Figure** 1: Examples of diagrams for direct (a) and resolved photon (b) processes in electron-proton scattering.

Predictions for the jet cross section are usually obtained in leading order (LO) QCD by convoluting the parton densities in the photon and in the proton with hard partonic scattering cross sections calculated at the tree level. The partons leaving the hard scattering reaction are identified with hadronic jets. Due to the reduced center of mass energy of the resolved reactions jet production from these processes could not be studied in detail in previous fixed target photoproduction experiments. At HERA energies however, the results of several authors [4] agree in predicting that the photoproduction of jets is dominated by resolved reactions at low and medium transverse energies $E_t^{jet}$ of the jets, say below 30 GeV. Thus, in the framework of this QCD picture, measurement of the jet cross section can be used to obtain information on the photon's parton content assuming the parton densities in the proton are known. From $e\gamma$ deep inelastic scattering experiments, studied at $e^+e^-$ colliders, the quark content of the photon is already relatively well known in the fractional momentum range of the parton $0.007 \leq x_\gamma \leq 1$ [5]. The photoproduction of jets at high energies therefore offers a new tool for the determination of the gluon density in the photon. Recent experiments which study jet production in $\gamma\gamma$ scattering are also sensitive to this quantity [6].

The present analysis studies 2-jet production with more than 7 GeV transverse energy $E_t^{jet}$ per jet in photon-proton scattering. The scattered electron is tagged at small angles so that the photon is almost real and the energy of the photon is known from $E_\gamma = E_{beam} - E_{tag}$. Inclusive differential cross sections $d\sigma/dp_t$ and $d\sigma/d\eta$ are derived at the leading order parton level. Here $p_t$ describes the transverse momenta of the partons and $\eta$ their pseudo-rapidities in the laboratory system. The unfolding method described below extracts partonic cross sections from the measured jet distributions utilizing a Monte Carlo model which besides the LO QCD model describes the influence of initial and final state parton showers, multiple parton interactions, hadronization and detector effects.

The results can be directly compared to LO calculations using different parametrizations for the parton densities. In next to leading order (NLO) QCD a jet algorithm has to be introduced at the parton level as well. The calculations presented so far [7, 8] take a cone algorithm and find differences between LO and NLO predictions of the order of only 10% – 30% for values of transverse jet energy, jet pseudo-rapidity and other jet parameters used in this paper.

Besides comparing the inclusive jet cross sections with theoretical predictions, the gluon density in the photon can also be derived in a more direct way. The momentum fraction $x_\gamma = E_{(parton/\gamma)}/E_\gamma$ can be fully reconstructed knowing the energies and angles of the jets and the energy of the incoming photon. By unfolding the measured $x_\gamma^{vis}$ distribution to the parton level using the same Monte Carlo model mentioned above and correcting for the quark contribution and the direct photon processes, it is therefore possible to determine the gluon density distribution in leading order.

The paper is structured as follows: after a short description of the detector and of the event selection, the Monte Carlo model used for comparisons with the data is studied with respect to the energy flow around jets. The model is then used to extract from the jets observed in the data inclusive parton cross sections at the leading order QCD level which can be directly compared to analytical QCD calculations. It is further used to determine a distribution of the fractional momentum $x_\gamma$ from 2-jet events which is interpreted in terms of a) the direct photon contributions, b) the resolved contributions with a quark from the photon, and c) the resolved contributions with a gluon from the photon.

## 2 Detector Description and Selection of 2-jet Events

A detailed description of the H1 apparatus can be found elsewhere [9]. The following briefly describes the components of the detector relevant for this analysis, which makes use of the calorimeters, the luminosity system and the central tracking detector.

The LAr calorimeter [10] extends over the polar angular range $4^\circ < \theta < 153^\circ$ with full azimuthal coverage, where $\theta$ is defined with respect to the proton beam direction ($+z$ axis). The calorimeter consists of an electromagnetic section with lead absorbers, corresponding to a depth of between 20 and 30 radiation lengths, and a hadronic section with steel absorbers. The total depth of the LAr calorimeter varies between 4.5 and 8 hadronic interaction lengths. The calorimeter is highly segmented in both sections with a total of around 45000 cells. The electronic noise per channel is typically in the range 10 to 30 MeV (1 $\sigma$ equivalent energy). Test beam measurements of LAr calorimeter modules have demonstrated energy resolutions of $\sigma(E)/E \approx 0.12/\sqrt{E} \oplus 0.01$ with $E$ in GeV for electrons [11] and $\sigma(E)/E \approx 0.5/\sqrt{E} \oplus 0.02$ for charged pions [9, 12]. The hadronic energy scale and resolution have been verified from the balance of transverse momentum between hadronic jets and the scattered electron in deep inelastic scattering events and are known to a precision of 5% and 10% respectively.

The calorimeter is surrounded by a superconducting solenoid providing a uniform magnetic field of 1.15 T parallel to the beam axis in the tracking region. Charged particle tracks are measured in two concentric jet drift chamber modules (CT), covering the polar angular range $15^\circ < \theta < 165^\circ$, and a forward tracking detector (FT), covering the range $7^\circ < \theta < 25^\circ$.

The luminosity system consists of two TlCl/TlBr crystal calorimeters having a resolution of $\sigma(E)/E = 0.1/\sqrt{E}$ with $E$ in GeV. The electron tagger is located at $z = -33$ m and the photon detector at $z = -103$ m. The electron tagger accepts electrons with an energy fraction between 0.2 and 0.8 with respect to the beam energy and scattering angles below $\theta' \leq 5$ mrad ($\theta' = \pi - \theta$).

The events used in this analysis were taken during the 1993 running period, in which HERA collided 26.7 GeV electrons on 820 GeV protons, and correspond to an integrated luminosity of 290 $\mathrm{nb}^{-1}$. They were triggered by a coincidence of the electron tagger and at least one track from the central jet chamber trigger. Events were selected, if they fullfilled the following criteria:

1. The energy deposited in the electron tagger was in the range $8 \leq E_{tag} \leq 20$ GeV. The cross sections refer to a scaled photon energy of $0.25 \leq y \leq 0.7$ and a negative squared four-momentum of the photon of $Q^2 \leq 0.01$ GeV$^2$. For the sample used to determine the inclusive parton cross sections an additional containment cut for the electron shower was applied in order to facilitate the acceptance calculation of the electron tagger.

2. At least one track in the central tracker with transverse momentum above 0.3 GeV coming from the interaction region was required to determine the position of the vertex along the beam axis.

3. The width of the vertex distribution along the beam axis was $\sigma = 10$ cm. Events were accepted in the region of $\pm 3$ standard deviations around the nominal vertex position.

Jet reconstruction was based on purely calorimetric measurements using a cone algorithm [13] in a grid of the azimuthal angle $\varphi^{cell}$ and pseudo-rapidity $\eta^{cell}$ which extends from $-3 \leq \eta^{cell} \leq 3$. The cone radius $R = \sqrt{\Delta\eta^2 + \Delta\varphi^2}$ in the standard analysis was chosen to be $R = 1.0$ and $R = 0.7$ was also used for cross checks. Jets were ordered according to the transverse energy in the cone. Events were accepted, if

1. At least 2 jets were found, each with transverse energy above $E_t^{jet} \geq 7$ GeV.

2. The jets were contained in the LAr calorimeter $0 \leq \eta^{jet} \leq 2.5$.

3. The rapidity difference between the two most energetic jets was less than $|\Delta\eta| \leq 1.2$ in order to reject events where the photon spectator (Fig.1b) is misidentified as a jet from the hard parton-parton scattering process.

The trigger efficiency was determined to be 94±1% using a monitoring trigger with full efficiency for this event selection. A correction of the jet energy scale with respect to the Monte Carlo model leads to an additional selection criterion which is described below. The total number of 2-jet events remaining is 366 without the cut on the shower containment in the electron tagger, and 292 for all cuts.

## 3 Monte Carlo Generator for QCD Processes

For the analysis of the data, the PYTHIA 5.6 event generator for photon-proton interactions [14] was used together with a generator for quasi-real photons. PYTHIA is based on leading order (LO) QCD matrix elements and includes initial and final state parton shower models. The strong coupling constant $\alpha_s$ was calculated in first order QCD using $\Lambda_{QCD} = 200$ MeV with 4 flavours. The renormalization and factorization scales were both set to the transverse momentum $p_t$ produced in the parton-parton scattering. Since the QCD calculation used here is divergent for processes with small transverse momenta of the partons emerging from the hard interaction a lower cut-off has been applied in PYTHIA. This was set to $p_t \geq 2$ GeV.

For the proton structure the GRV-LO [15] leading order parton density parametrizations were used. The GRV-LO [16] leading order parametrizations were used for the photon structure. The latter give a consistent description of the data as will be shown below. Optionally, PYTHIA allows for additional interactions within the same event. These are LO QCD processes between partons from the photon remnant and partons from the proton remnant. This so called *multiple interaction* option has been explored in proton-antiproton collisions before [14, 17] and the same parameters have been used here. For the hadronization process the LUND fragmentation scheme was applied (JETSET [18]).

The detector response for the generated events was simulated with a detailed simulation program and then reconstructed with the same program as used for the data. The generated events therefore allow the calculation of correlations between the jets reconstructed in the detector and the underlying parton kinematics (see below). These correlations will be used to study the parton-parton scattering processes with the jets observed in the data.

## 4 Energy Flow in Jet Events

The precision of the measurement of the transverse jet energy $E_t^{jet}$ and how well the jet energy correlates with the parent parton momentum $p_t$ are critical matters. This is because the transverse jet energy distributions fall like $(E_t^{jet})^{-n}$ where $n \sim 5.5$ [2] so that an imperfect description of the energy flow around the jet direction by the Monte Carlo model is a potential source of serious error in the conclusions on the parton scattering process. The fact prevented relevant conclusions on the photon structure in previous publications [1, 2, 3] and is taken into account in this paper for the first time at HERA.

In Fig.2a the observed transverse energy flow around the jet direction per event is shown versus the rapidity distance from the jet axis in a slice of $|\varphi^{cell} - \varphi^{jet}| \leq 1$. As an example jets were selected with transverse energy $7 \leq E_t^{jet} \leq 8$ GeV collected in a cone of size $R = 1$ and pseudo-rapidity between $0 \leq \eta^{jet} \leq 1$. The jet profiles are asymmetric, showing a higher energy level in the direction of the proton ($\Delta\eta \geq 0$) compared to the photon direction ($\Delta\eta \leq 0$). It is interesting to note that the energy flow depends not only on rapidity, but also on the momentum fraction $x_\gamma$ of the parton from the photon side. The parton momentum fraction can be reconstructed using the two jets with the highest transverse energy $E_t^{jet}$ in the event and their pseudo-rapidities $\eta^{jet}$ together with the energy of the photon $E_\gamma$:

$$x_\gamma^{vis} = \frac{E_t^{jet1} e^{-\eta^{jet1}} + E_t^{jet2} e^{-\eta^{jet2}}}{2E_\gamma} \tag{1}$$

The jet profiles are shown in two bins of $x_\gamma^{vis}$, above and below 0.4. Two effects are observed:

1. In the photon direction ($\Delta\eta \leq 0$) the low $x_\gamma^{vis}$ data show an enhanced energy flow relative to the high $x_\gamma^{vis}$ data. This can be ascribed to the remnant particles of the photon which should be reduced at high $x_\gamma$, and absent altogether in the case of direct photon processes for which $x_\gamma = 1$.

2. In the proton direction ($\Delta\eta \geq 0$) the energy flow is also enhanced in the low $x_\gamma^{vis}$ distribution compared with the high $x_\gamma^{vis}$ data. This increased energy flow indicates additional event activity for events with small parton momenta $x_\gamma$, or large energies $\sim (1 - x_\gamma)$ of the photon spectators.

The jet core is narrower in the case of the high $x_\gamma^{vis}$ sample compared to the low $x_\gamma^{vis}$ sample. This effect is connected to the energy flow around the jet and the jet energy interval: since the

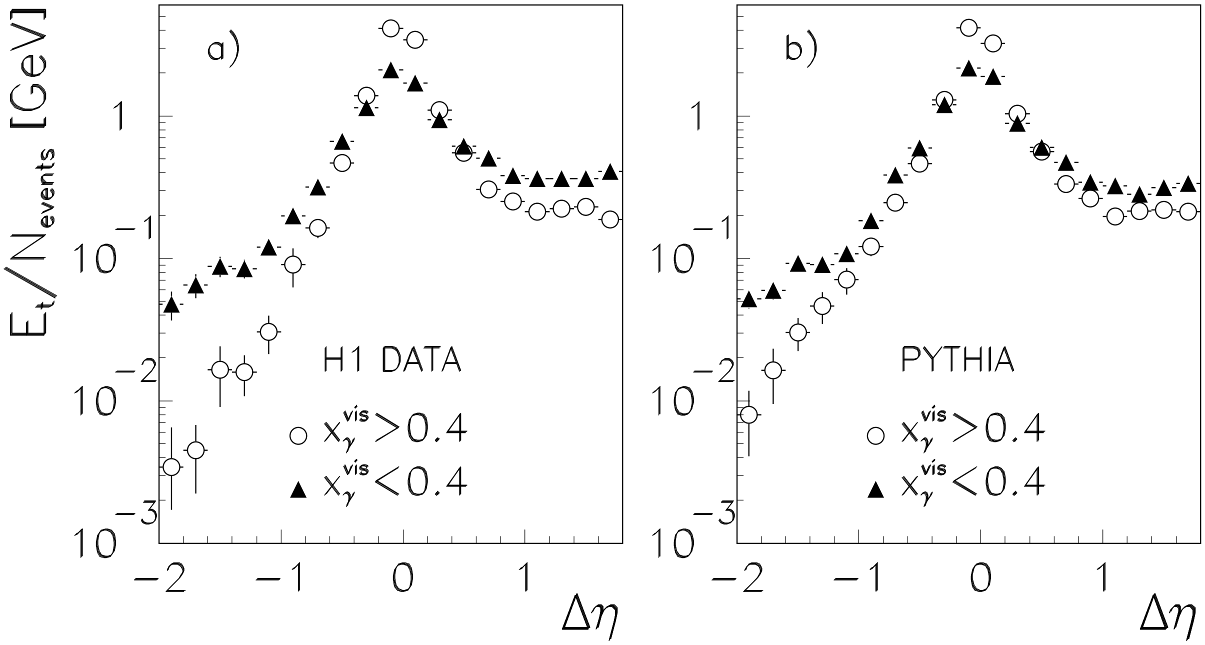

**Figure** 2: Observed transverse energy flow versus the rapidity distance from the jet direction (integrated over $|\varphi^{cell} - \varphi^{jet}| \leq 1$) for a) data and b) PYTHIA with multiple interactions. The jets were selected with transverse energy $7 \leq E_t^{jet} \leq 8$ GeV in a cone of size $R = 1$ and jet rapidities between $0 \leq \eta^{jet} \leq 1$. The energy flow depends on the momentum fraction $x_\gamma$ of the parton from the photon: shown are large $x_\gamma^{vis} \geq 0.4$ (open circles) and small $x_\gamma^{vis} \leq 0.4$ (filled triangles).

jets were required to have $\sim 7$ GeV in the cone, a reduced energy flow around the jet enforces more energy in the core.

In Fig.2b the transverse energy flow is shown for events of the PYTHIA model including multiple interactions. The model also shows an excess of low $x_\gamma^{vis}$ over high $x_\gamma^{vis}$ data at positive as well as at negative rapidities.

The observed transverse energy flow in the azimuthal angle $|\Delta\varphi|$ around the jet direction is shown in Fig.3a,c for two bins of the jet rapidity. The energy flow has been integrated in a slice of $|\eta^{cell} - \eta^{jet}| \leq 1$ around the jet axis. The transverse energy of the jets was again restricted to $7 \leq E_t^{jet} \leq 8$ GeV summed in a cone of size $R = 1$. The H1 data are shown as full circles. The observed energy flow outside of the jet cone is much higher for jets at large rapidities $2 \leq \eta^{jet} \leq 2.5$ (Fig.3c) compared to jets in the central detector region $0 \leq \eta^{jet} \leq 0.5$ (Fig.3a) and is increasing in between $0.5 \leq \eta^{jet} \leq 2$ (not shown). Due to the cut on the rapidity difference of the two jets $|\Delta\eta| \leq 1.2$ a part of the second jet is always seen at $\Delta\varphi \sim \pi$.

The average transverse energy flow per cone area $\pi R^2$ determined outside of the jet cone provides a measure of the *jet pedestal*, often called underlying event [19]. This jet pedestal is later used to estimate the amount of energy inside the jet cone which is, according to the PYTHIA model with multiple interactions, not due to the fragmentation of the hard scattered partons. The pedestal energy was determined event by event in the slice $|\eta^{cell} - \eta^{jet}| \leq 1$ and $|\varphi^{cell} - \varphi^{jet}| \geq 1$. Regions affected by the second jet were excluded from the measurement. The distributions of the jet pedestals corresponding to the jet profiles of Fig.3a,c are shown in Fig.3b,d.

The PYTHIA model without additional interactions (dashed line) does not give a good description of the jet profiles and pedestal distributions. In this model the pedestal energy corresponds to QCD radiation and fragmentation effects. The QCD radiation effects are approximately taken into account by the parton shower models included in PYTHIA.

The PYTHIA model with multiple interactions provides an improved description of the jet shapes, which is reasonable in the rapidity range $0 \leq \eta^{jet} \leq 0.5$, but shows deviations from the data at large jet rapidities $2 \leq \eta^{jet} \leq 2.5$. The differences between data and Monte Carlo model are still too large to be neglected. Moreover the sometimes large contributions of energy due to multiple interactions in the jet cone give a poor correlation between parton and jet energies because this contribution leads to events entering the $E_t^{jet} \geq 7$ GeV sample which have parton transverse momentum below the cutoff used in the Monte Carlo model, namely 2 GeV.

In order to avoid this problem the transverse energies of the jets in the data were reduced by the average pedestal difference between data and PYTHIA without multiple interactions. In this way the jets were only corrected for the additional energy flow over and above the initial and final state radiation and fragmentation effects. A corresponding pedestal subtraction was applied to the jets of the PYTHIA events with multiple interactions. The corrections were parametrized in terms of the rapidity of the jets so as to match the effect seen in the data. The corrections vary between $0.3 - 2.3$ GeV for the data and $0.3 - 1.3$ for the events of the PYTHIA model with multiple interactions. This subtraction evidently also corrects for the difference in the pedestal energies between Monte Carlo and data, provided that this energy difference is the same on average inside and outside the cone; which would be the case for multiple interactions. As an additional safeguard the transverse energy of the jets is required to be above $E_t^{jet} \geq 7$ GeV even after this jet pedestal correction which ensures that the parent parton transverse momentum exceeds 2 GeV. In all figures of the following sections these jet energy corrections will be applied to data events and Monte Carlo events.

Overall, the multiple interaction option gives an improved description of the energy flow and offers a natural explanation of the observed effects. However, the improved description of the

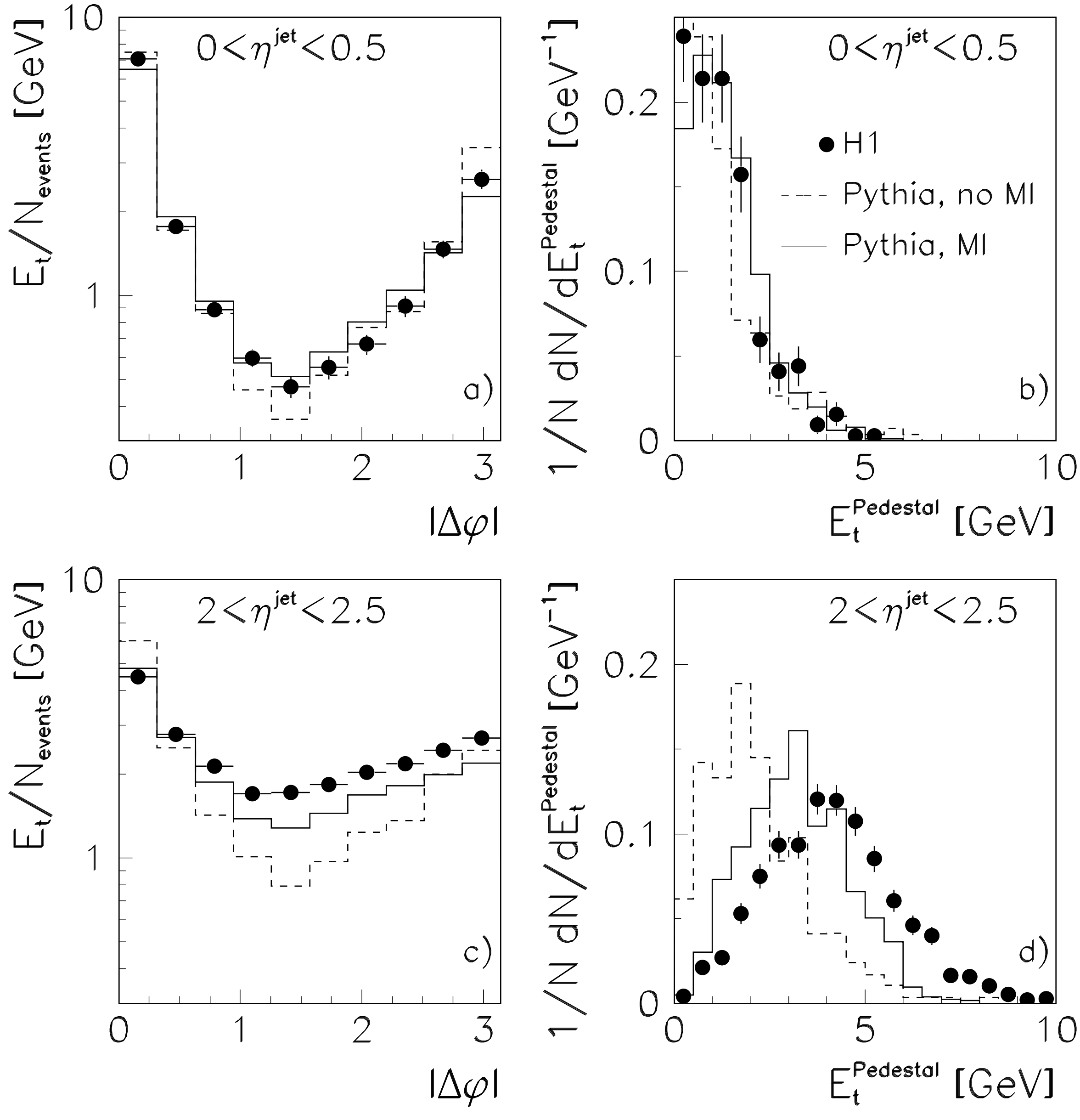

**Figure** 3: a,c) Observed transverse energy flow versus the azimuthal angle with respect to the jet direction (integrated over $|\eta^{cell} - \eta^{jet}| \leq 1$) in two rapidity bins: a) $0 \leq \eta^{jet} \leq 0.5$ and c) $2 \leq \eta^{jet} \leq 2.5$. The jets have transverse energies $7 \leq E_t^{jet} \leq 8$ GeV in a cone of size $R = 1$. Full circles are H1 data. The histograms refer to PYTHIA events with (full line) and without (dashed line) multiple interactions. b,d) Distribution of the transverse energy measured outside of the jets in the slice $|\eta^{cell} - \eta^{jet}| \leq 1$, normalized to the area $\pi R^2$.

jet shape by this model cannot be considered as a definite proof of the existence of multiple interactions. Therefore a model dependence remains in this analysis where the PYTHIA version with multiple interactions is used to extract direct information from the observed jet spectra on the underlying (LO) parton-parton scattering processes.

## 5 Jet-Parton Correlations

The predicted correlations obtained with PYTHIA between jet and leading order parton quantities are shown in Fig.4: a) for azimuthal angles $\varphi$; b) for pseudo-rapidities $\eta$; c) for the transverse jet energy $E_t^{jet}$ and the parton transverse momentum $p_t$; and d) for the reconstructed parton momentum fraction from the photon side (Equation 1) with respect to the true $x_\gamma$ at the parton-parton scattering process. In the leading order picture, two hard partons exist per event, and there are at least two jets. Therefore for the $\varphi$, $\eta$, and $p_t$ distributions the jet with the highest $E_t^{jet}$ was correlated with the parton giving the smallest invariant jet-parton mass, and the second jet with the other parton.

Also, in the case of $x_\gamma^{vis}$ (Fig.4d), the two highest $E_t^{jet}$ jets were used. According to the nominator of (1), different values of $x_\gamma^{vis}$ correspond to different 2-jet configurations: small values of $x_\gamma^{vis}$ require two jets with large rapidities and small transverse jet energies. Here the remaining jet pedestal, discussed in Section 4 (dashed line of Fig.3c), raises $x_\gamma^{vis}$ relative to the true $x_\gamma$. Events with large $x_\gamma^{vis}$ have at least one of the jets at small rapidity or large transverse jet energies. At small rapidities the remaining jet pedestal is small relative to the total $E_t^{jet}$ (dashed line of Fig.3a), and $x_\gamma^{vis}$ corresponds in average to the true $x_\gamma$. At $x_\gamma \sim 1$ transverse energy deposited outside of the jets reduce $x_\gamma^{vis}$ relative to the true $x_\gamma$. The photon energy in the denominator of (1) was precisely determined from the energy of the scattered electron measured in the electron tagger system. The resolution in the logarithm of the reconstructed parton momentum fraction is approximately Gaussian in $log_{10}(x_\gamma) - log_{10}(x_\gamma^{vis})$ and varies between 0.22 at true parton momenta around $x_\gamma \sim 0.05$ and 0.16 at $x_\gamma \sim 0.5$.

From the study of the jet-parton correlations, the momenta of the hard partons can be reconstructed from the measured jet energies. It is then possible to extract partonic cross sections and leading order parton densities. The cross sections can be compared directly to leading order QCD calculations instead of smearing the theoretical cross section with transverse momenta of the partons inside the proton and the photon, QCD radiation effects, fragmentation, detector effects, jet formation, and then confronting it with the data.

In principle such an unfolding procedure seems to be straightforward. The distribution of an observable $g^{det}$ measured by the detector is related to the distribution of a partonic observable $f^{part}$ by an integral equation which expresses the convolution of the true distribution with all effects between the creation of the hard parton and the measurement process $g^{det}(u) = \int A(u,w) f^{part}(w) dw$. This integral equation can be transformed to a matrix equation. Solving this matrix equation thus leads directly to the histogram $f^{part}(w)$ and therefore e.g. to the partonic cross section. This simple method can produce spurious oscillating components in the result due to the limited detector resolution. Therefore the method has to be improved by a regularization procedure which reduces the resulting correlations by optimizing both the number and position of the bins for the unfolded variable.

In the analysis presented here an unfolding method [20] has been used to determine the differential cross section $d\sigma/dp_t$ and to derive the distribution of the parton momentum $x_\gamma$. Because the resolution in the transverse momentum $p_t$ is much worse than the resolution in rapidity $\eta$, for the extraction of $d\sigma/d\eta$ the transverse momentum $p_t$ is unfolded for three different bins in $\eta$. The $p_t$ integrated results then give the inclusive cross section $d\sigma/d\eta$.

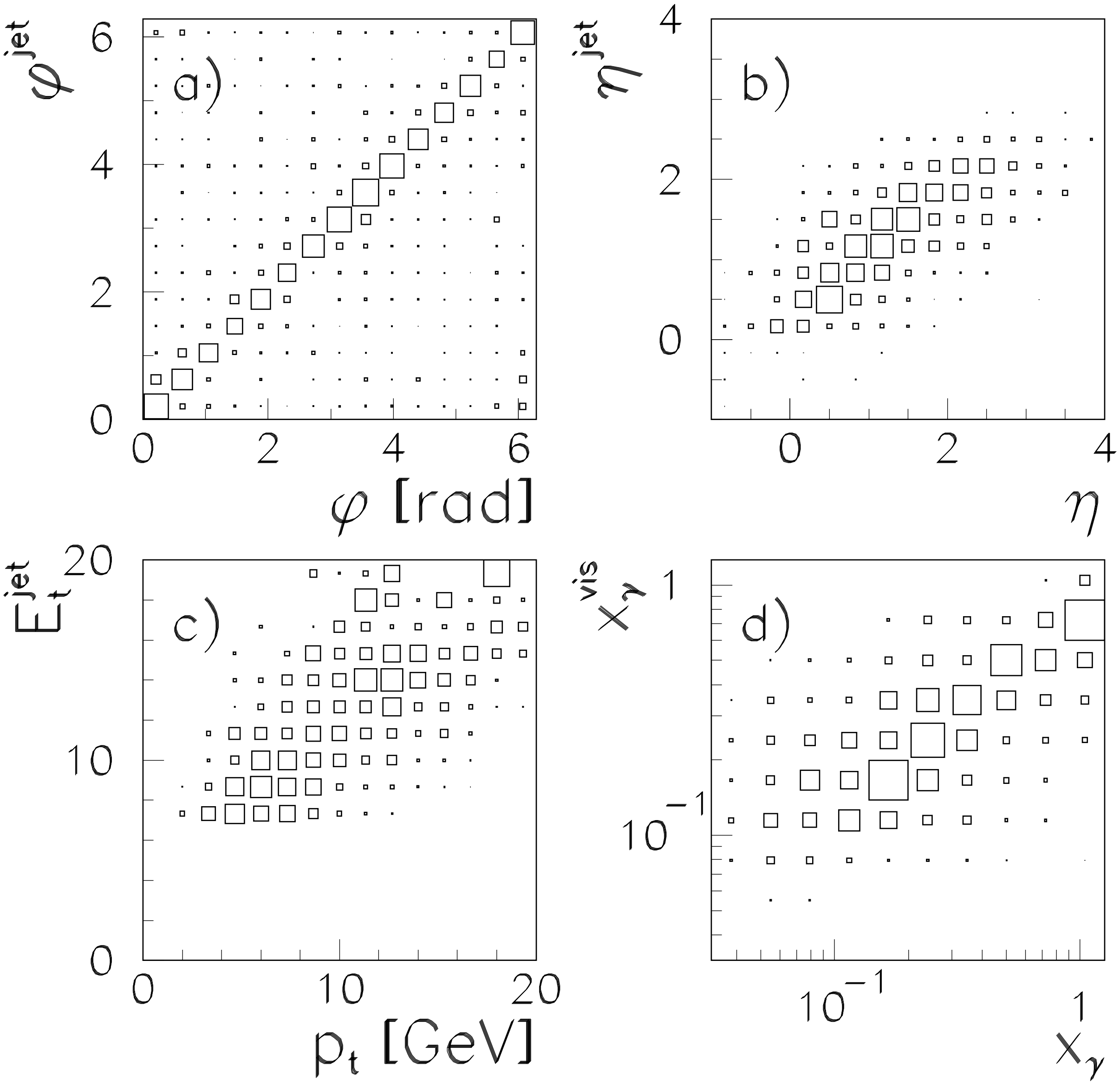

**Figure** 4: Correlations between reconstructed jets and leading order parton quantities according to PYTHIA with multiple interactions: a) azimuthal angle $\varphi$, b) rapidity $\eta$, c) transverse parton momentum $p_t$ (to account for the steeply falling distribution the histogram has been weighted with the transverse jet energy $(E_t^{jet})^4$ ), d) momentum fraction $x_\gamma$ of the parton from the photon side.

Technically, the unfolding procedure delivers a weight for each Monte Carlo event in terms of the true value of the observable chosen for the unfolding which then can be used to reweight Monte Carlo distributions of different variables. The comparison of these distributions with the data give an important check of the transformation, as described in the Monte Carlo simulation, between the partonic distributions and the measurable distributions. An accurate Monte Carlo description of this transformation is essential for a reliable unfolding.

## 6 Parton Cross Sections

In Fig.5 the unfolded single inclusive parton $ep$ cross section $d\sigma/dp_t$ is shown. The integration over the parton rapidity $0 < \eta < 2.5$, the initial photon energy and momentum transfer squared has already been carried out. The unfolding was done in the $p_t$ variable alone. Migration effects in $p_t$ influence the result in the lowest $p_t$ bin most strongly. In order to minimize these effects an option in the algorithm was used which allows to constrain the cross section in the bin $4 \leq p_t \leq 7$ GeV (not shown in the figure) to a reasonable extrapolation of the results shown in the figure. In addition, it ensures small bin to bin correlations (less than 30%) and a smooth behaviour of the reweighting function. Because the $p_t$ distribution is steeply falling, the largest systematic error stems from an error in the determination of the calorimetric energy. Variations of the constraint on the cross section in the unseen bin and other unfolding parameters result in a 20% error on the cross section shown in the figure. Because the result is given in the parton rapidity range $0 \leq \eta \leq 2.5$, but the correlation used for unfolding is for all parton rapidities, an additional systematic error of 25% is included to account for a possible difference in the correlations of the full and the restricted sample. Other systematic error sources are described in Section 7. The error bars are computed from the quadratic addition of statistical and systematic errors. The cross section, statistical and systematic errors can be found in Table 1.

The solid line in Fig.5 is the result of a leading order calculation [21] using the GRV parton densities in leading order QCD for the proton and the photon. The factorization and renormalization scales are given by $p_t^2$. The QCD parameter $\Lambda$ was set to 200 MeV. Leading order calculations for other photon parametrizations (LAC1: dashed line, LAC3: dotted line [22]) are also included. A NLO QCD calculation has been carried out by the same authors [21] using the GRV higher order parton densities in the photon and the proton, the 2-loop calculation of $\alpha_s$, $\Lambda^{(4)}_{\overline{MS}} = 200$ MeV, and a cone size of $R = 1$. Compared to the LO calculation the NLO calculation is essentially larger by an overall factor 1.25.

As discussed in the previous Section an important check of the success of the transformation consists in the comparison of a set of measured observables with the result of the reweighted Monte Carlo simulation. This is shown in Fig.6. The distribution of the measured transverse jet energy $E_t^{jet}$ is well described by the Monte Carlo simulation after reweighting (solid line). Because the initial set of parameters already gives a good description of the data (dashed line) the new weights differ only slightly from one. Also the agreement between the data and the model in other variables like $\eta^{jet}$ for all jets and $\eta^{jet1} + \eta^{jet2}$ for the two highest $E_t^{jet}$ jets (Figs. 6 b,c) is at a satisfactory level.

The unfolded inclusive parton $ep$ cross section $d\sigma/d\eta$ is shown in Fig.7 together with the theoretical predictions. Statistical and systematic errors are treated in the same way as in Fig.5. The flat shape of the distribution is well reproduced by the LO QCD calculations using the three parametrizations of the photon structure function as above. The absolute rate is consistent with the calculation using the GRV parametrization. The NLO QCD calculation again is larger by an overall factor 1.25 with respect to the LO calculation.

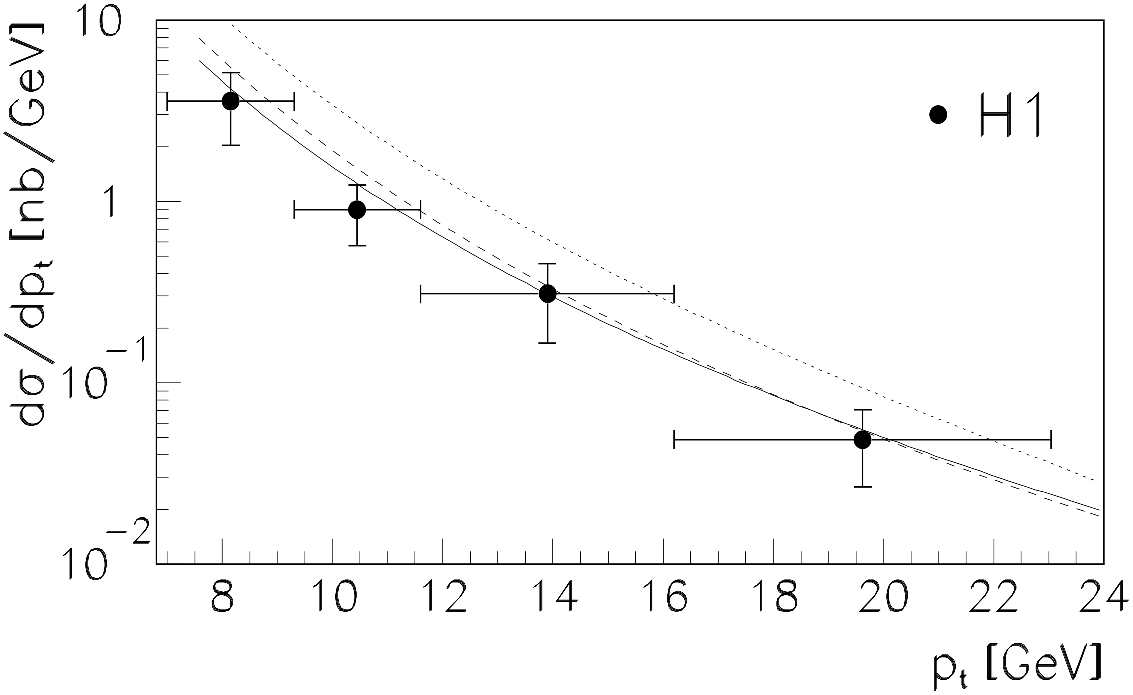

**Figure** 5: Single inclusive parton *ep* cross section unfolded to the leading order partonic matrix element versus transverse momentum $p_t$ for $0 < \eta < 2.5$. The solid line is the partonic cross section obtained from a leading order QCD calculation [21] using the GRV leading order parton densities for the proton and the photon. For the dashed (dotted) line the photon parton densities are taken from the LAC1 (LAC3) parametrization.

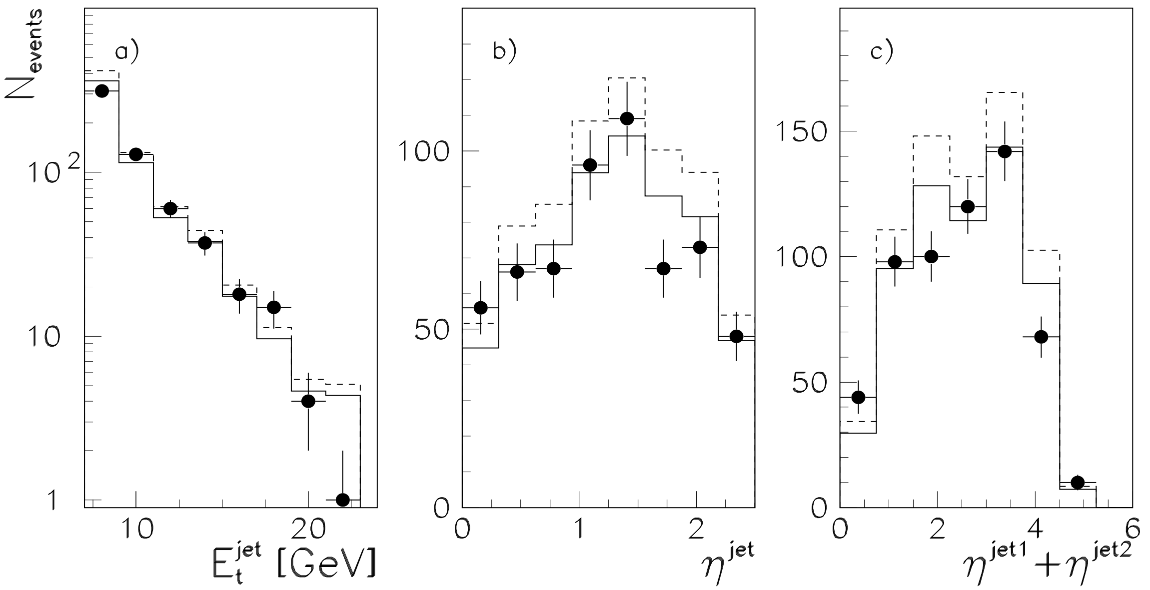

**Figure** 6: Distributions for the unfolding of $p_t$. Shown is the comparison of data on detector level with the Monte Carlo model after (solid line) and before (dashed line) reweighting. The parton densities are taken from the GRV parametrizations. a) The $E_t^{jet}$ distribution of the jets, b) the pseudo-rapidity distribution of the jets, c) the distribution of $\eta^{jet1} + \eta^{jet2}$ for the two highest $E_t^{jet}$ jets.

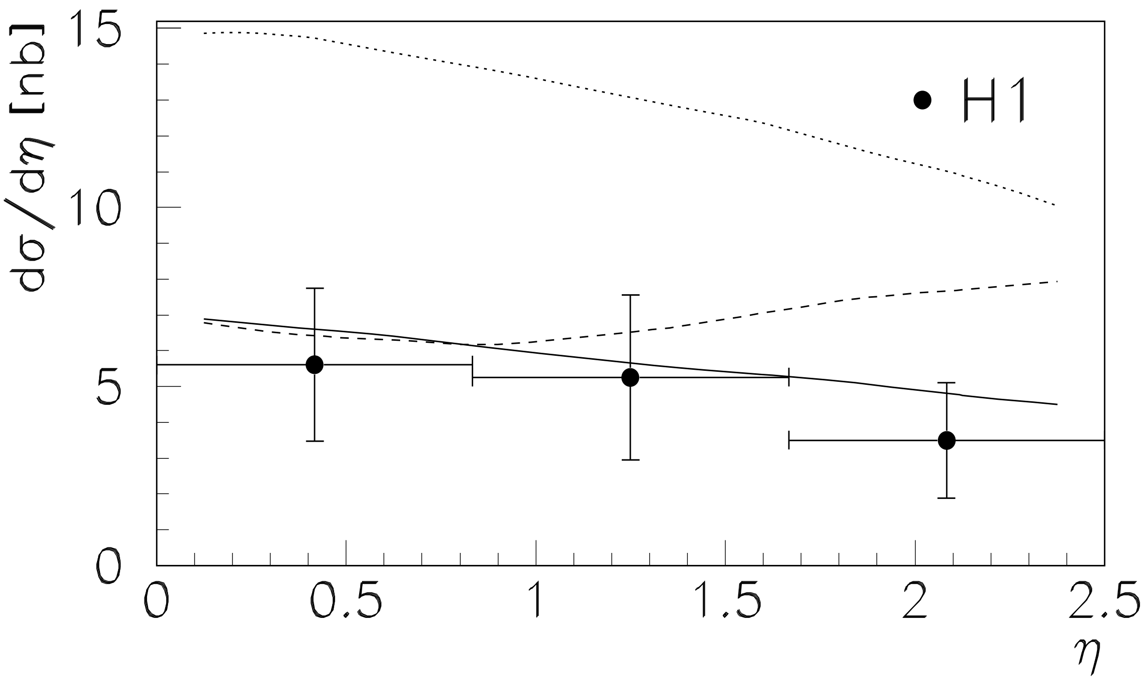

**Figure** 7: Single inclusive parton $ep$ cross section unfolded to the leading order partonic matrix element versus pseudo-rapidity $\eta$ for $p_t > 7$ GeV. The solid line is the partonic cross section obtained from a leading order QCD calculation [21] using the GRV leading order parton densities for the proton and the photon. For the dashed (dotted) line the photon parton densities are taken from the LAC1 (LAC3) parametrization.

# 7 Parton Momentum Distributions in the Photon

In this Section the full 2-jet kinematics is used to check the validity of the leading order QCD description of the hard scattering process and to extract information on the subprocesses which contribute to the observed jet rate. This will finally allow the determination of parton densities in the photon as a function of $x_\gamma$. The main goal is to derive, for the first time, the gluon momentum distribution $x_\gamma g(x_\gamma)$ in the photon over a large range in $x_\gamma$.

The correlation between true and reconstructed parton momenta is shown in Fig.4d. The migration effects are large, so the unfolding procedure - described in Section 5 - is used to correct from the reconstructed $x_\gamma^{vis}$ to the true $x_\gamma$ distribution. As explained before, the unfolding enforces agreement with the $x_\gamma^{vis}$ distribution (Fig.8a), whereas the agreement of the reweighted distributions of other variables simulated by the Monte Carlo model with the actually observed data distributions (Fig.8b-d) delivers important checks of the transformation:

1. Fig.8b) the fraction of the parton momentum from the proton side was determined using $x_p^{vis} = 0.5 \left( E_t^{jet1} e^{\eta^{jet1}} + E_t^{jet2} e^{\eta^{jet2}} \right) / E_p$. For most of the events $x_p^{vis}$ is above 0.01 where the quark content of the proton is well established by lepton-nucleon scattering experiments and the gluon content is known to a level of 15%.
2. Fig.8c) the difference in the rapidities of the jets is related to the scattering angle $\Theta^*$ of the partons in the CM frame of the parton-parton scattering process: $\tanh(|\eta^{jet1} - \eta^{jet2}|/2) = \cos\Theta^*$. The distributions of $\cos\Theta^*$ are predicted by LO QCD for all combinations of the interacting partons. This is a basic QCD prediction which has to be fullfilled.
3. Fig.8d) the differences in the transverse energies of the jets are large compared to the experimental resolution and reflect large average transverse momenta of the incident partons. Initial state radiation effects are important and to a smaller extent large transverse energies of the photon remnant.

The distributions in Fig.8b-d demonstrate that a leading order Monte-Carlo model for the hard scattering process is able to give a consistent description of the observed 2-jet events by adjusting only the photon structure function. Higher order effects as described by initial state parton showers and multiple interactions to describe the enhanced energy flow at large rapidities are however essential to describe the data.

Fig.9 shows the unfolded $x_\gamma$ distribution compared to calculations of the PYTHIA generator. The full line represents the prediction of the resolved photon processes with a quark on the photon side at the hard parton-parton scattering process. The quark distribution in the photon as determined by two photon experiments is input in the form of the GRV-LO parametrization [16]. The quark induced processes contribute mainly to the central region of the distribution corresponding to parton momenta around $x_\gamma = 0.5$.

The prediction of the direct processes are shown as a dashed line above $x_\gamma \geq 0.77$. They account for 3/4 of the events in the highest $x_\gamma$ bin. Together with the quark component the size of the direct photon calculation, using the GRV-LO parametrization of the parton densities in the proton, is consistent with the data at large $x_\gamma$.

At small parton momenta $x_\gamma \leq 0.2$ the contribution of events initiated by a quark from the photon as predicted by the given model is clearly below that seen in the data. This suggests explaining the additional events at small $x_\gamma$ by gluons entering the hard process from the photon side.

By subtracting the predicted direct and resolved quark contributions from the data the event distribution of the gluon contribution remains. Comparison with the distribution calculated for

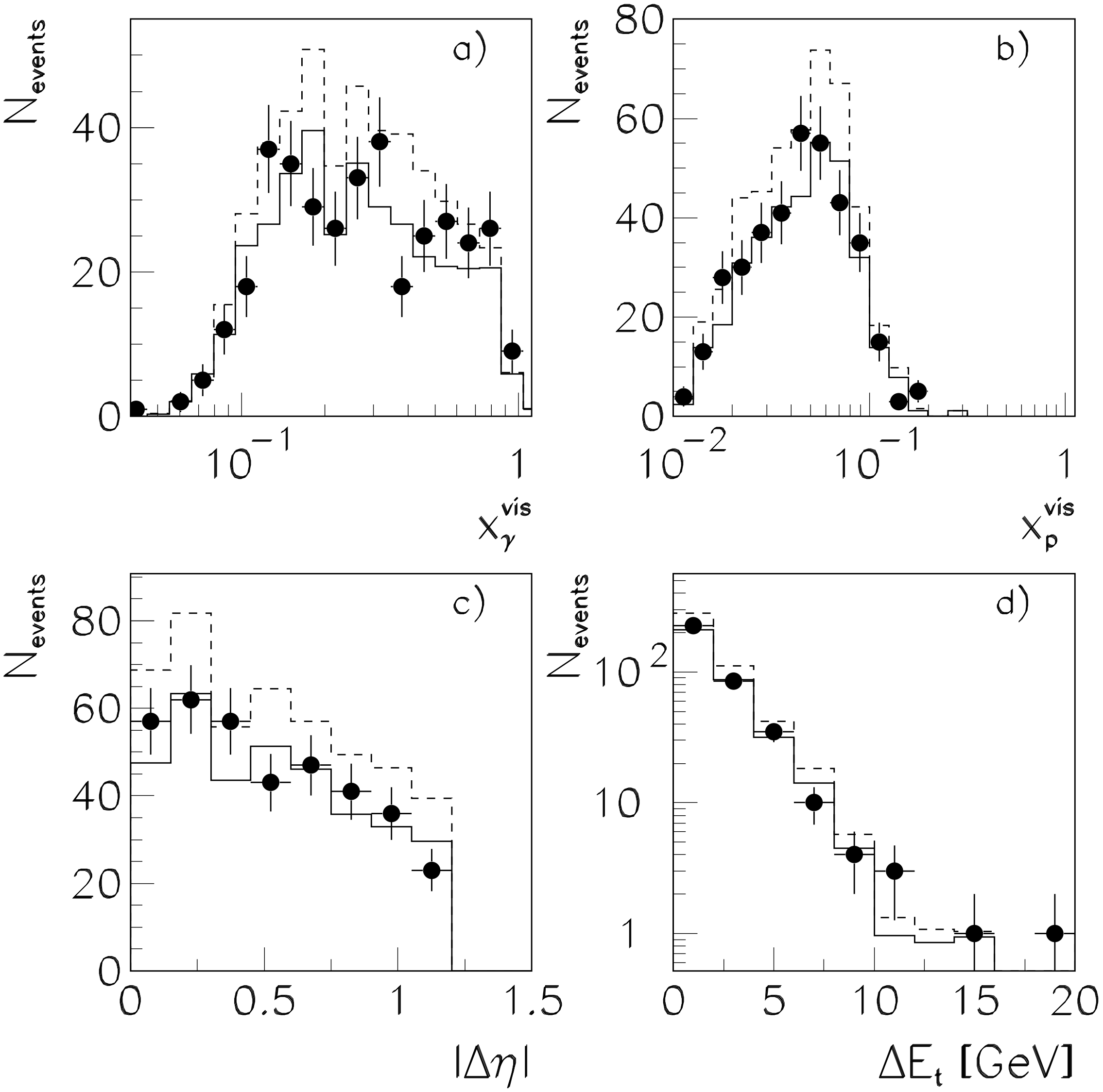

**Figure** 8: Distributions of the 2-jet data (circles) are compared with the PYTHIA calculations before (dashed line: absolute prediction) and after (full line) the reweighting procedure: a) momentum fraction of the parton from the photon $x_\gamma^{vis}$, b) momentum fraction of the parton from the proton $x_p^{vis}$, c) difference in the jet rapidity $|\eta^{jet1} - \eta^{jet2}|$ which is a measure of the scattering angle in the parton-parton system, and d) the difference in the jet transverse energy $|E_t^{jet1} - E_t^{jet2}|$.

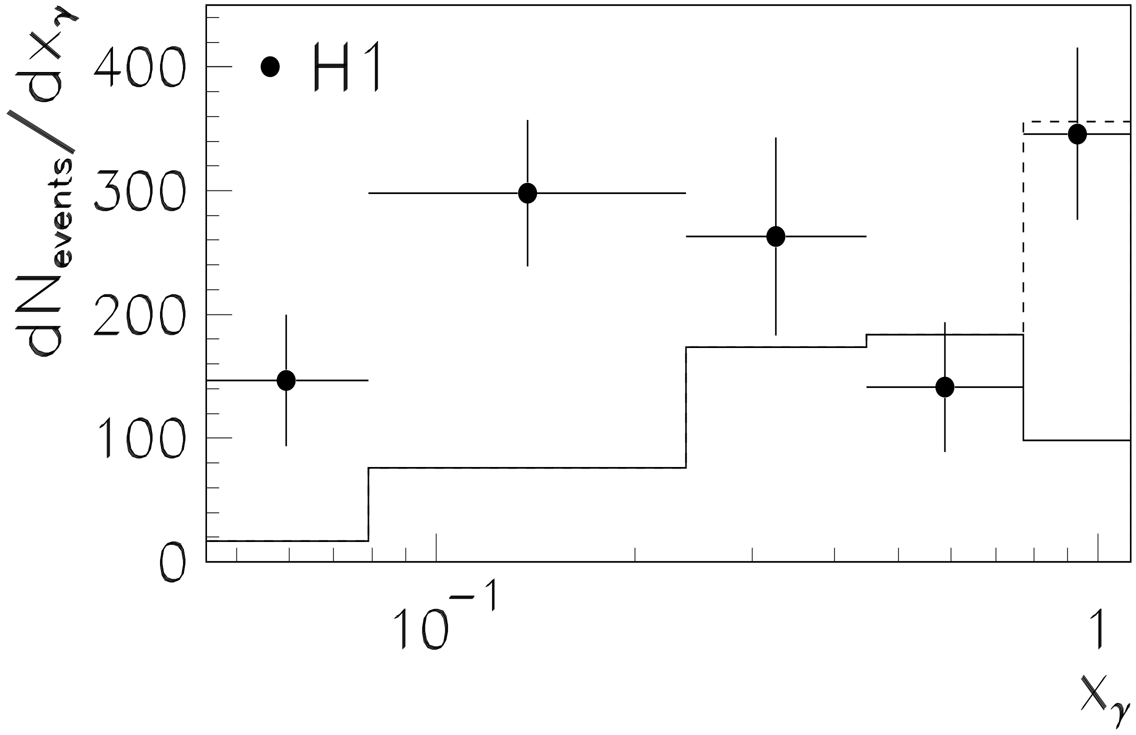

**Figure** 9: 2-jet event distribution (points) of the true fractional momentum $x_\gamma$ of the parton from the photon. Only the statistical errors are shown. The full line represents the predicted contribution of the quark resolved photon processes, the dashed line shows the size of the direct photon calculation as obtained by the PYTHIA Monte Carlo.

processes initiated by a gluon from the photon side, yields correction factors to be applied to the modelled distribution. The resulting gluon density is shown in Fig.10 (see also Table 1): the total errors include statistical and systematic errors where all contributions have been added in quadrature. The systematic errors were calculated from the following sources:

1. Error in knowledge of the calorimeter energy scale of ±5%.
2. The statistical error in the determination of the hadronic pedestal correction of ±10%.
3. Uncertainty in the quark density of the photon estimated conservatively as ±30%.

The systematic errors are dominated at small $x_\gamma$ values by errors 1 and 2, whereas at high values of $x_\gamma$ error 3 is as large as errors 1 and 2. An additional error from the luminosity measurement of 5% is not included in the Fig.10.

To check whether or not a gluon content in the photon is needed to explain the observed rate in the data, the following test was carried out using the $x_\gamma^{vis}$ distribution: the observed data rate in Fig.9 was reduced by lowering the energy scale of the calorimeter according to the error source 1. The remaining sample was further reduced by subtracting more energy from each jet according to error source 2. The Monte Carlo prediction for processes with a quark from the photon however was raised according to the uncertainty given in item 3 above. With the assumption that no gluon exists in the photon the remaining data events were compared in a $\chi^2$ test to the predicted number of quark and direct events of the Monte Carlo calculatio giving a probability below 0.1% for this hypothesis. Thus, a gluon contribution in the photon is needed to explain the observed data

The average parton transverse momentum of the selected events is $< p_t >^2 = 75$ GeV$^2$ where $p_t$ is used as factorization and renormalization scale for the QCD calculation. A change of $\Lambda$ from 200 MeV to 300 MeV reduces the parton density by 30%. A variation of the gluon density in the proton by ±15% [23] changes the gluon density in the photon by ∓15%.

The gluon density in the photon in Fig.10 is compared to the parametrizations of GRV-LO[16], LAC1 and LAC3[22]. A high gluon density at large parton momenta, as suggested by the LAC3 parametrization, is clearly excluded. This is consistent with previous observations at HERA [2], TRISTAN and LEP [6]. Above $x_\gamma \geq 0.08$ both the GRV-LO and LAC1 parametrizations of the gluon distribution are consistent with the data. The strong rise of the LAC1 parametrization below $x_\gamma \leq 0.08$ is not supported, while the GRV-LO distribution is consistent with the data. In the latter model the gluon distribution of the photon is essentially generated by QCD radiation.

## 8 Conclusion

Photoproduction processes with at least two high $E_t^{jet}$ jets in the final state were studied with the H1 detector. The jet quantities as observed in the detector were unfolded to leading order parton quantities using jet-parton correlations based on a specific version of the PYTHIA QCD generator. Within the present experimental errors the data are – after a correction of the jet energy – consistent with this leading order description of the hard scattering process together with higher order processes in the initial and final state and multiple interactions, i.e. interactions between partons of the photon and proton spectators.

Single inclusive differential *ep* parton cross sections were derived as a function of the transverse momentum $p_t \geq 7$ GeV and pseudo-rapidity $0 \leq \eta \leq 2.5$ of the partons for photon energies corresponding to $0.25 \leq y \leq 0.7$ and momentum transfer below $Q^2 \leq 0.01$ GeV$^2$. They agree

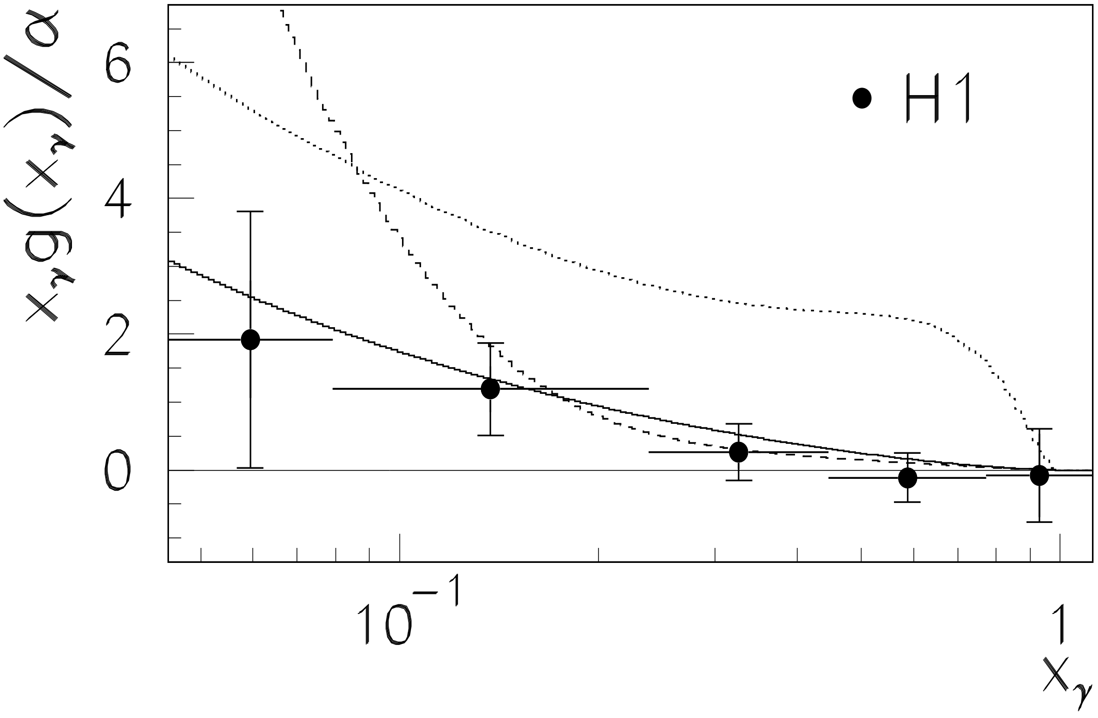

**Figure** 10: The gluon density of the photon divided by the fine structure constant $\alpha = 1/137$ (data: circles) at the scale $< p_t >^2 = 75$ GeV$^2$. For comparison the GRV-LO (full) and the LAC1 (dashed) and the LAC3 (dotted) parametrizations are shown.

| $p_t$ [GeV] | 8.2 | 10.5 | 13.9 | 19.6 |
|---|---|---|---|---|
| $d\sigma/dp_t$ [nb/GeV] | 3.57 | 0.90 | 0.31 | 0.049 |
| $\sigma_{stat}$ | 0.19 | 0.09 | 0.05 | 0.013 |
| $\sigma_{syst}$ | 1.52 | 0.32 | 0.13 | 0.018 |

| $\eta$ | 0.42 | 1.25 | 2.08 |
|---|---|---|---|
| $d\sigma/d\eta$ [nb] | 5.61 | 5.25 | 3.50 |
| $\sigma_{stat}$ | 0.37 | 1.02 | 0.16 |
| $\sigma_{syst}$ | 2.10 | 2.07 | 1.60 |

| $x_\gamma$ | 0.059 | 0.14 | 0.33 | 0.59 | 0.93 |
|---|---|---|---|---|---|
| $x_\gamma g(x_\gamma)/\alpha$ | 1.92 | 1.19 | 0.26 | -0.12 | -0.08 |
| $\sigma_{stat}$ | 0.87 | 0.34 | 0.24 | 0.15 | 0.61 |
| $\sigma_{syst}$ | 1.68 | 0.59 | 0.33 | 0.33 | 0.30 |

**Table** 1: Single inclusive differential parton cross sections (Fig.5,7) and the gluon distribution in the photon (Fig.10) together with their statistical and systematic errors.

well with QCD predictions. A direct study of 2-jet kinematics was used to determine the momentum fraction of the partons from the photon. At large $x_\gamma$ it is consistent with the predictions of the direct component plus the resolved component initiated by quarks from the photon. At low parton momentum fraction the observed jet rate in the data can only be explained by a gluon component in the photon. For the first time a leading order gluon distribution was derived down to $x_\gamma = 0.04$. The average scale was $< p_t >^2 = 75$ GeV$^2$ corresponding to the mean transverse momentum squared of the final state partons. Gluon distributions with high density at large $x_\gamma$ or steeply rising gluon distributions at small $x_\gamma$ are disfavoured.

### Acknowledgement

We are grateful to the HERA machine group whose outstanding efforts made this experiment possible. We appreciate the immense effort of the engineers and technicians who constructed and maintain the H1 detector. We thank the funding agencies for financial support. We acknowledge the support of the DESY technical staff. We wish to thank the DESY directorate for the support and hospitality extended to the non-DESY members of the collaboration.

## References

[1] H1 Collab., T. Ahmed et al., Phys. Lett. B297 (1992) 205

[2] H1 Collab., I. Abt et al., Phys. Lett. B314 (1993) 436

[3] ZEUS Collab., M. Derrick et al., Phys. Lett. B297 (1992) 404
ZEUS Collab., M. Derrick et al., Phys. Lett. B342 (1995) 417
ZEUS Collab., M. Derrick et al., "Dijet Cross Sections in Photoproduction at HERA", DESY-95-033 (1995)

[4] W. J. Stirling, "Proceedings of the HERA Workshop", ed.R.D.Peccei, Hamburg 1987 and references therein

M. Klasen, G. Kramer, S.G. Salesch, "Photoproduction of jets at HERA: Comparison of next-to-leading order calculation with ZEUS data", DESY-94-232 (1994)

[5] Ch. Berger and W. Wagner, Phys.Rep.146 (1987) 1
Opal Collab., R. Akers et al., Z. Phys. C61 (1994) 199

[6] AMY Collab., B.J. Kim et al., Phys. Lett. B325 (1994) 248
TOPAZ Collab., H. Hayashii et al., Phys. Lett. B314 (1993) 149
ALEPH Collab., D. Buskulic et al., Phys. Lett. B313 (1993) 509
DELPHI Collab., P. Abreu et al., Phys. Lett. B342 (1995) 402

[7] L.E. Gordon, J.K. Storrow, Phys. Lett. B291 (1994) 320
M. Greco, A. Vicini, Nucl. Phys. B415 (1994) 386

[8] G. Kramer, S.G. Salesch, Z. Phys. C61 (1994) 277
D. Bödeker, G. Kramer, S.G. Salesch, Z. Phys. C63 (1994) 471

[9] H1 Collab., I. Abt et al., "The H1 detector at HERA", DESY preprint 93-103 (1993), to be submitted to Nucl. Instr. and Meth.

[10] H1 Calorimeter Group, B. Andrieu et al., Nucl. Instr. and Meth. A336 (1993) 460

[11] H1 Calorimeter Group, B. Andrieu et al., Nucl. Instr. and Meth. A350 (1994) 57

[12] H1 Calorimeter Group, B. Andrieu et al., Nucl. Instr. and Meth. A336 (1993) 499

[13] J. E. Huth et al., Fermilab-Conf-90/249-E (1990)

[14] T. Sjöstrand, CERN-TH-6488 (1992), Comput. Phys. Commun. 82 (1994) 74

[15] M. Glück, E. Reya and A. Vogt, Z. Phys. C53 (1992) 127

[16] M. Glück, E. Reya and A. Vogt, Z. Phys. C53 (1992) 651

[17] AFS Collab., T. Akesson et al., Z. Phys. C34 (1987) 163
UA2 Collab. J. Alitti et al., Phys. Lett. B268 (1991) 145
CDF Collab. L.J. Keeble et al., "A Study of four jet events and search for double parton scattering at $\sqrt{s} = 1.8$ TeV.", FERMILAB-CONF-92-161-E (1992)

[18] T. Sjöstrand, M. Bengtsson, Comput. Phys. Commun. 43 (1987) 367

[19] S.D.Ellis, Proceedings "QCD and High Energy Hadronic Interactions", 28th Rencontre de Moriond, Ed. J. Tran Thanh Van, Editions Frontieres (1993) 235

[20] V. Blobel, DESY 84-118, and Proceedings of the 1984 CERN School of Computing, Aiguablava (Spain), CERN 1985

[21] M. Klasen and S.G. Salesch, calculations based on [8] (1994)

[22] H. Abramowicz, K. Charchula, A. Levy, Phys. Lett. B269 (1991) 458

[23] NMC Collab., M.Arneodo et al., Phys. Lett. B309 (1993) 222